

Article

The Structural Design of and Experimental Research on a Coke Oven Gas Burner

Mingrui Geng, Suyi Jin and Denghui Wang * 

School of Energy and Power Engineering, Xi'an Jiaotong University, Xi'an 710049, China; gmr11@stu.xjtu.edu.cn (M.G.); suyijin2019@163.com (S.J.)

* Correspondence: denghuiwang@163.com

Abstract: A novel low-NO_x burner was proposed in this study to achieve the stable and clean combustion of low- and medium-calorific-value gas and promote energy sustainability, and the influence of the gas pipe structure on the burner's characteristics was studied with coke oven gas as a fuel. A 40 kW burner test bench was established to conduct cold-state experiments to investigate the influences of the gas pipe structure on the aerodynamic characteristics of the burner. We performed numerical simulations on both a 40 kW burner and a 14 MW prototype burner to investigate the thermal performance of the burners and their impact on low NO_x emissions. The experimental results showed that increasing the deflection angle of the gas pipe nozzle direction relative to the circumferential tangent direction, the high-velocity zone and the high-concentration zone of the flow field move towards the central axis. Increasing the bending angle of gas pipe nozzle direction relative to the axis direction caused the high-velocity zone and the high-concentration zone to move upstream direction of the jet. The simulation reveals that the NO concentration at the exit cross-section of the combustion chamber of the 14 MW prototype burner is 17.00 mg/m³ (with 3.5% oxygen content). A recommended design structure of the burner was proposed, with a deflection angle of 0° and a bending angle of 0° for the No. 3 gas pipe, and a deflection angle of 15° and a bending angle of 30° for the No. 4 gas pipe.

Keywords: gas burner; low calorific value gas; coke oven gas; NO_x; numerical simulation



Citation: Geng, M.; Jin, S.; Wang, D.

The Structural Design of and Experimental Research on a Coke Oven Gas Burner. *Sustainability* **2024**, *16*, 4185. <https://doi.org/10.3390/su16104185>

Academic Editor: Janusz Kozinski

Received: 17 April 2024

Revised: 11 May 2024

Accepted: 15 May 2024

Published: 16 May 2024



Copyright: © 2024 by the authors. Licensee MDPI, Basel, Switzerland. This article is an open access article distributed under the terms and conditions of the Creative Commons Attribution (CC BY) license (<https://creativecommons.org/licenses/by/4.0/>).

1. Introduction

In industrial production, low- and medium-calorific-value gases mainly include coke oven gas, blast furnace gas, low-calorific-value coalbed gas, and Linz–Donawitz gas [1–4]. Due to the low combustible gas content and the presence of inert gases such as CO₂ and N₂ in low- and medium-calorific-value gas, combustion issues such as difficulties with ignition, low combustion stability, and incomplete combustion often occur [5–7]. The substantial reserves of low- and medium-calorific-value gas for comprehensive recycling hold significant importance in energy conservation, emission reduction, and ecological protection [8,9].

Coke oven gas is the main by-product of the coke-making industry, with the production of 1 ton of coke yielding 300–360 m³ of coke oven gas [10–12]. In 2015, China's coke production amounted to approximately 378 million tons, and this figure had surged to around 473 million tons by 2022 [13]. In China, in addition to approximately 50% of coke oven gas being returned to the furnace for heating and self-consumption, over a quarter of the coke oven gas is not recycled, leading to energy waste and nitrogen oxide pollution [9,14]. In recent years, the Chinese government has consistently introduced environmental protection policies [15], steadily raising the emission standards for flue gases from gas boilers. In Beijing, the nitrogen oxide emission limit for newly constructed gas boilers is set at or below 30 mg/m³, referred to as ultra-low NO_x emissions [16]. This has resulted in higher demands on the clean combustion and utilization of gaseous fuels.

In addressing these issues, Zhang et al. [17] conducted a systematic analysis of the combustion stability of low-calorific-value gas in a hot air heating furnace. The results indicated that gas composition and the equivalence ratio significantly influence combustion stability. Cai et al. [18] conducted structural modifications on a low calorific value coalbed methane burner, accelerating the rise in flame temperature along the central axis and reducing its length. This modification resulted in an increased local volumetric heat load. Through experimental research, Bâ et al. [19] demonstrated that preheating reactants effectively enhances the stability of the oxygen-enriched combustion of blast furnace gas and widens the combustion limits. Karyeyen et al. [20] conducted experiments on the combustion of low-calorific-value gas under turbulent premixed combustion conditions. The results indicated that a premixed gas composed of blast furnace gas and air can achieve stable combustion when hydrogen is introduced. Weiss et al. [21] utilized numerical simulation methods to predict the reactions of coke oven gas in the heating system of a coke oven.

NO_x in boiler flue gas falls into three categories: thermal, fast, and fuel based. Thermal NO_x results from the oxidation of N₂ in the high-temperature combustion environment. Zeldovich's mechanism [22,23] suggests that thermal NO_x production surges significantly above 1773 K, increasing by 6 to 7 times per 100 K rise in temperature. In studies on low-NO_x combustion, Zhong et al. [24] pointed out that, during the combustion process of coke oven gas, thermal NO_x accounted for 95% of the NO_x emission value in the flue gas. Cao et al. [25] investigated the influence of the internal flue gas recirculation window structure on the NO_x concentration at the exit of the combustion chamber, using coke oven gas as the fuel. The results indicated that the emission concentration of NO was relatively influenced by the average temperature, maximum flame temperature, and temperature uniformity within the combustion chamber. Poraj et al. [26] discovered that air-staging combustion technology has a significant inhibitory effect on NO generation through a study of the coke oven heating system. Paubel et al. [27] proposed a novel burner suitable for low-calorific-value gas, which realized the non-premixed combustion of blast furnace gas, methane, and oxygen. This experiment investigated the combustion characteristics of burners within the range of 30% to 90% of the volumetric fraction of blast furnace gas in the gas mixture and a 0% to 100% oxygen concentration in the central pipe. The results indicated that the net calorific value of the gas has a significant impact on the flame morphology.

Previous studies have frequently focused on adjusting combustion process parameters, yet there is limited literature on low-NO_x burners that are suitable for low- and medium-calorific-value gas, particularly regarding the precise design and optimization of burner structures. This study introduces a novel low-NO_x burner suitable for coke oven gas. Experimental research on the cold-state flow characteristics of the different gas pipe structures in the burner was conducted with the aim of providing essential scientific data for the optimal design of burners for low- and medium-calorific-value gas.

2. Burner Model and Experimental Methods

2.1. The Novel Low-NO_x Gas Burner Proposed in This Paper

The newly developed low-NO_x gas burner investigated in this study uses coke oven gas as combustion fuel. As shown in Figure 1, the burner optimizes the spatial distribution of gas and air by adopting air cyclone and gas dispersion jet technology. Combustion air is fed axially into the burner from the burner end face, while an air tangential cyclone structure is arranged at the burner outlet. The center of the cyclone structure is a direct current (DC) duct, and the outer ring area is a tangential cyclone blade at an angle of 30° to the axial direction. This cyclone structure divides the air into three parts: center DC air passing through the center DC duct, cyclone air passing through the cyclone vanes, and peripheral DC air passing through the outer edge. The center DC air ensures stable ignition and combustion of the central gas, while the cyclone air enhances turbulence intensity, promoting the mixing of gas and air. The peripheral DC air compensates for the

rigidity shortcomings of the cyclone air, improving flame stability. Gas is introduced from the upper part of the burner, and after being distributed by the distribution ring, it is fed into the combustion chamber through several gas supply pipes. Gas is distributed by the distribution ring and then fed into the combustion chamber through several gas pipes.

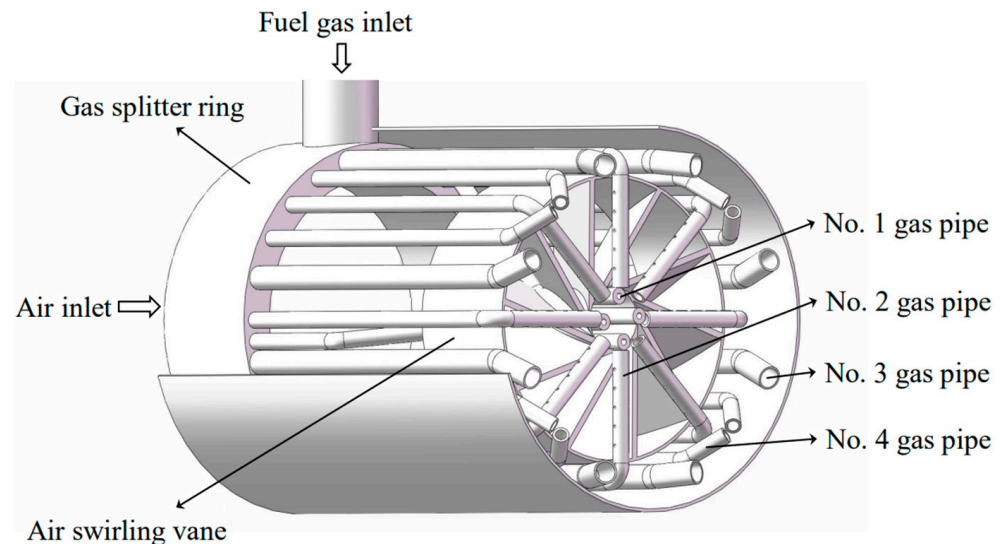


Figure 1. Schematic diagram of the structure of a novel low- NO_x gas burner.

In order to conduct laboratory-scale test experiments, it is important to reduce the complexity of the burner prototype through modeling. Following to the similarity theory [28], during the cold-state test of aerodynamic field, it was essential to ensure (1) geometric similarity between the model and the prototype; (2) that the airflow dynamics characteristics fall within the second self-modelling region; and (3) consistent momentum-fluid rate ratios for each gas nozzle between the model and the prototype. The purpose of this study was to explore the trends in the impact of the burner's structural parameters on the aerodynamic field, rather than a precise regulation of burner performance based on prototype dimensions. Consequently, the gas flow inlet structure and the number of gas pipes were simplified appropriately to facilitate burner processing.

The burner model, designed for a power of 40 kW, is schematically depicted in Figure 2. Air is drawn in through four air inlets at the inlet end of the burner, while an air tangential cyclone structure is positioned at the outlet end. The gas inlet is located at the inlet end of the burner, and the gas pipes are divided into four groups according to the different positions and sizes. The No. 1 gas pipe, situated at the center of the cyclone structure, ensures flame stability. Six No. 2 gas pipes form a ring-shaped array perpendicular to the central axis at the pipe's end, each featuring six symmetrically arranged gas nozzles along the pipe wall, enhancing gas–air mixing. Additionally, six No. 3 and No. 4 gas pipes are symmetrically positioned on either side of the No. 2 gas pipe to achieve dispersed combustion.

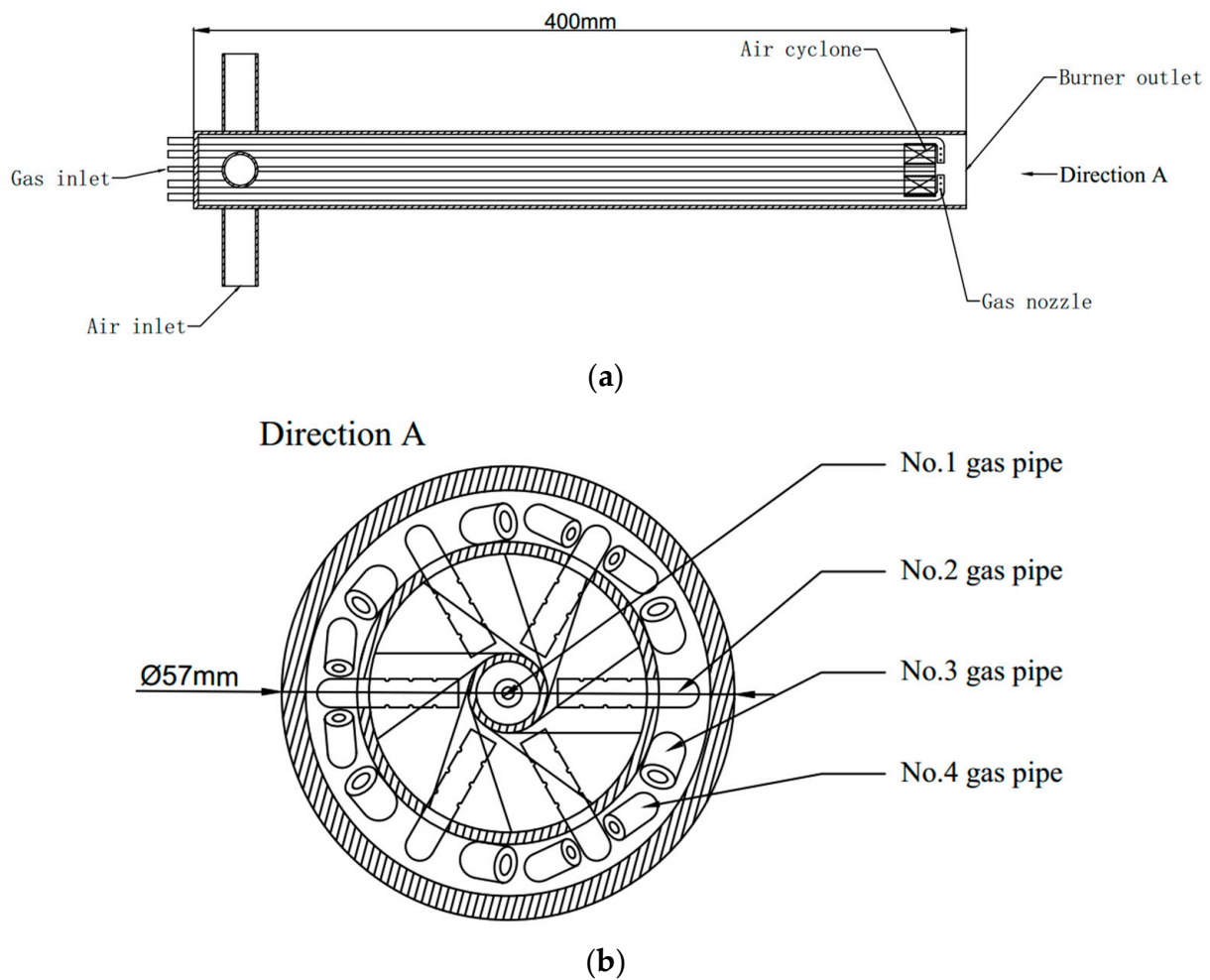


Figure 2. Schematic structure of the new low-NO_x burner model. (a) Overall burner structure; (b) gas pipe structures.

2.2. Test System

2.2.1. Cold-State Test System

According to the approximate formulae provided in the literature [29] for the flame length and diameter of oil (gas) burners, a cylindrical combustion chamber with dimensions of 230 mm in diameter and 700 mm in length was designed based on the burner power. The gas consumption for burner operation at rated conditions is $8.6 \text{ m}^3 \cdot \text{h}^{-1}$ and the air consumption is $39.21 \text{ m}^3 \cdot \text{h}^{-1}$. A diagram of the system for the cold-state test is shown in Figure 3. The required air was supplied by an axial-flow air compressor, and the gas was replaced by a mixture of carbon dioxide and air, which was mixed by a mixer and fed into the gas pipe. Each air supply pipe was equipped with a float flow meter to regulate and monitor the air flow. The burner's aerodynamic field was measured using S-type Pitot tubes and a testo 512 differential manometer with a full-scale measurement accuracy of 0.5% and a resolution of 0.1 m/s, while the gas concentration field was measured using a Gamet dx4000 FTIR analyzer (Gaset Technologies Oy, Helsinki, Finland) with a full-scale measurement accuracy of 1% and a resolution of 1 ppm. Table 1 displays the rated operating parameters of the burner.

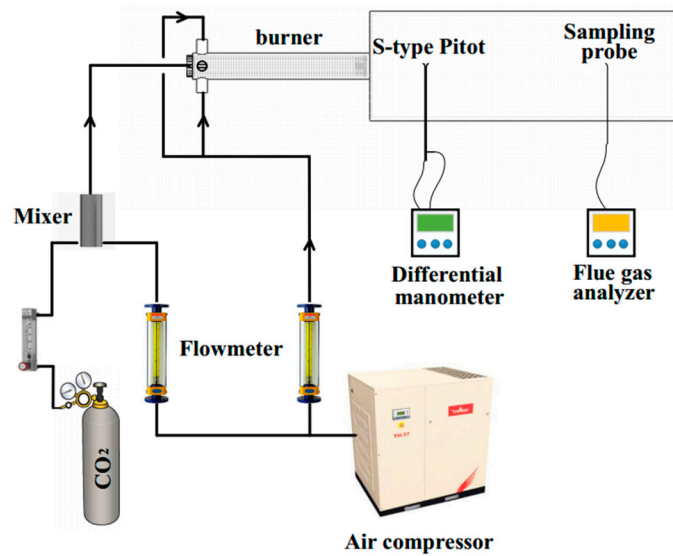


Figure 3. Cold-state test system diagram.

Table 1. Rated operating parameters of the burner.

Number	Name	Symbol	Unit	Value
1	Excess air factor	α	1	1.05
2	Gas consumption	V_{fuel}	$\text{m}^3 \cdot \text{h}^{-1}$	8.60
3	Air consumption	V_{air}	$\text{m}^3 \cdot \text{h}^{-1}$	39.21
Air distribution ratio				
4	Center DC air rate	η_{D1}	%	2.51
5	Cyclone air rate	η_{D2}	%	54.47
6	Peripheral DC air rate	η_{D3}	%	43.02
Gas distribution ratio				
7	No. 1 pipe gas volume share	η_1	%	3.39
8	No. 2 pipe gas volume share	η_2	%	19.57
9	No. 3 pipe gas volume share	η_3	%	56.64
10	No. 4 pipe gas volume share	η_4	%	20.40

2.2.2. Measurement Point Arrangement

In order to accurately measure the aerodynamic and gas concentration fields in the combustion chamber, 14 rows of measurement points are arranged in the axial direction in the combustion chamber as shown in Figure 4. An approximate value of 50 mm for the inner diameter d of the burner outlet is taken as the reference distance, thus defining the dimensionless radius as $R = r/d$ and the dimensionless axial distance of the measurement points as $X = x/d$. r is the distance from the center axis where the measurement point is located/mm. x is the distance from the measurement point to the burner nozzle cross-section/mm.

Since the flow field near the burner nozzle changes violently and the velocity gradient is large, the measurement points are arranged more closely. As the transition from the center of the burner nozzle to the two sides and downstream of the combustion chamber occurs, the measurement points become gradually sparser. The spacing Δr and the distance Δx between neighboring sections of each measurement section are shown in Table 2.

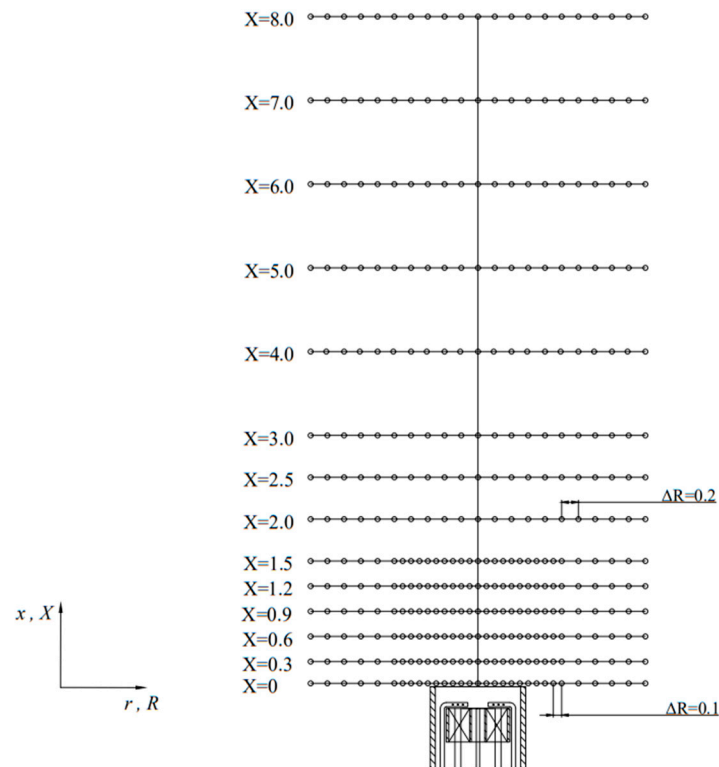


Figure 4. Cold-state test measurement point layout diagram.

Table 2. Distribution table of measurement cross-section spacing Δx and measurement point arrangement spacing Δr .

Number	X	$\Delta x/\text{mm}$	$\Delta r/\text{mm}$
1	0	/	5, 10
2	0.3	15	5, 10
3	0.6	15	5, 10
4	0.9	15	5, 10
5	1.2	15	5, 10
6	1.5	15	5, 10
7	2.0	25	10
8	2.5	25	10
9	3.0	25	10
10	4.0	50	10
11	5.0	50	10
12	6.0	50	10
13	7.0	50	10
14	8.0	50	10

In the gas concentration field measurement, the gas mixing is faster and the focus is on the gas concentration distribution near the burner nozzle, so the cross-section measurement points in the range of $0.0 < X < 4.0$ were measured.

2.3. Design of Test Conditions

The cold test primarily examined the impact of different angle designs of No. 3 and No. 4 gas pipes on the aerodynamic field and gas concentration field of the burner. The specifics of No. 3 and No. 4 gas nozzles are shown in Figure 5. The deflection angle of the nozzle direction for the No. 3 gas pipe is represented as β relative to the circumferential tangent direction, while the bending angle is represented as α relative to the axial direction. Similarly, the deflection angle of the nozzle direction for the No. 4 gas pipe is represented

as λ relative to the circumferential tangent direction, with the bending angle as θ relative to the axial direction. The arrangement of all the test conditions is outlined in Table 3.

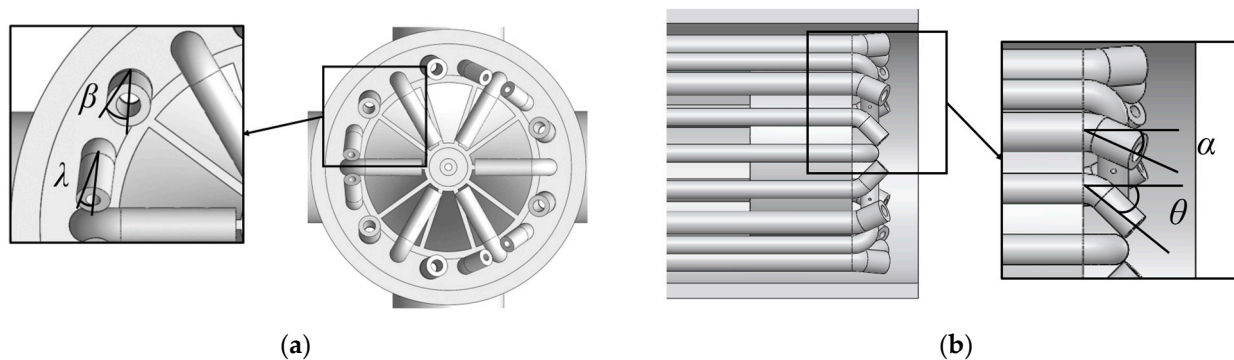


Figure 5. Schematic diagram of gas pipe nozzle structure. (a) Gas pipe deflection angle; (b) gas pipe bending angle.

Table 3. Cold-state test condition. The bending angle of No. 3 gas pipe α , the deflection angle of No. 3 gas pipe β , the bending angle of No. 4 gas pipe θ , the deflection angle of No. 4 gas pipe λ .

Group	Case	No. 3 Gas Pipe		No. 4 Gas Pipe		Clarification
		α	β	θ	λ	
1	0000	15°	0°	45°	15°	Original structure
	0101	15°	40°	45°	15°	Increase β
	0102	15°	65°	45°	15°	
	0103	15°	90°	45°	15°	
2	0201	15°	0°	45°	40°	Increase λ
	0202	15°	0°	45°	65°	
	0203	15°	0°	45°	90°	
3	0301	0°	0°	45°	15°	Increase α
	0302	30°	0°	45°	15°	
	0303	45°	0°	45°	15°	
4	0401	15°	0°	0°	15°	Increase θ
	0402	15°	0°	15°	15°	
	0403	15°	0°	30°	15°	

2.4. Data Processing

2.4.1. Dimensionless Velocity

The equivalent velocity obtained by dividing the total air and gas volume by the burner outlet cross-sectional area is taken as the reference velocity v_{eq} , defined as:

$$v_{eq} = \frac{V_{air} + V_{fuel}}{\pi d^2 / 4} \quad (1)$$

where v_{eq} is the equivalent velocity/ $\text{m}\cdot\text{s}^{-1}$; V_{air} is the air flow rate/ $\text{m}^3\cdot\text{s}^{-1}$; V_{fuel} is the gas flow rate/ $\text{m}^3\cdot\text{s}^{-1}$; d is the inner diameter of the burner outlet/50 mm.

The measured airflow velocity value v is divided by v_{eq} to obtain the dimensionless velocity, defined as $U = v/v_{eq}$.

2.4.2. Dimensionless Fuel–Air Ratio

A gas mixture of air and carbon dioxide is used to replace the gas in the cold-state test. In order to eliminate the influence of the original carbon dioxide in the air on the test

measurements, the fuel–air ratio φ (i.e., the volume ratio of the gas to the air) is introduced to characterize the mixing of gas and air.

$$\varphi = \frac{X}{Y} = \frac{z - n}{m - z} \quad (2)$$

where m is the carbon dioxide content of the gas (i.e., the mixture of air and carbon dioxide); n is the carbon dioxide content of the air; z is the carbon dioxide content at the measurement point in the combustion chamber; and X and Y are the volumes of the gas and air at the measurement point, respectively.

Taking the total gas volume fed to the burner divided by the total air volume obtained from the reference fuel–air ratio φ_0 as a reference, the dimensionless fuel–air ratio is defined as $\Phi = \varphi/\varphi_0$.

The larger the value of the dimensionless fuel–air ratio (Φ), the higher the gas concentration at the measurement point. When the gas is well mixed with air, the value of the dimensionless fuel–air ratio should be close to one.

2.4.3. Cross-Sectional Uniformity Index

The value of the cross-section uniformity index is between 0 and 1. Larger values indicate that the gas is more evenly distributed across the cross-section. It is defined as follows:

$$\gamma = 1 - \frac{\sum_{i=1}^n \frac{\sqrt{(\varphi_i - \bar{\varphi})^2}}{\bar{\varphi}} \cdot A_i}{2 \cdot A} \quad (3)$$

where γ is the cross-section uniformity index; φ_i is the local fuel–air ratio of the measurement point; $\bar{\varphi}$ is the average fuel–air ratio of the cross-section; A_i is the local grid area of the measurement point; A is the total grid area of the measurement cross-section; n is the total number of measurement points of the cross-section.

Among them, the cross-section average fuel–air ratio is defined as:

$$\bar{\varphi} = \frac{\sum_{i=1}^n \varphi_i \cdot A_i}{A} \quad (4)$$

2.4.4. Evaluation of Uncertainties

Experimental results are prone to errors, mainly stemming from accuracy errors in the measuring instruments and the imprecision of experimental measurement points. Among these, errors from measuring instruments and experimental procedures are unavoidable, necessitating the minimization of the impact of errors on experimental uncertainty. It is necessary to conduct measurements 3 to 5 times for each dataset, and ultimately take the arithmetic mean.

2.5. Numerical Model

2.5.1. Continuity Equation

The continuity equation can be expressed as follows:

$$\frac{\partial \rho}{\partial t} + \nabla \cdot (\rho \vec{v}) = 0 \quad (5)$$

where ρ is gas density/kg·m⁻³; t is time/s; v is velocity/m·s⁻¹.

2.5.2. Momentum Equation

The momentum conservation equation can be written in the following form:

$$\frac{\partial}{\partial t} (\rho \vec{v}) + \nabla \cdot (\rho \vec{v} \vec{v}) = -\nabla p + \nabla \cdot \left(\vec{\tau} \right) + \rho \vec{g} + \vec{F} \quad (6)$$

where p is static pressure/Pa; τ is stress tensor; g is gravitational acceleration/ $\text{m}\cdot\text{s}^{-2}$; F is external volume force/ $\text{N}\cdot\text{m}^{-3}$.

The stress tensor τ is determined by the following equation:

$$\overline{\tau} = \mu \left[\left(\nabla \vec{v} + \nabla \vec{v} \right) - \frac{2}{3} \nabla \cdot \vec{v} I \right] \quad (7)$$

where μ is molecular viscosity/ $\text{N}\cdot\text{s}\cdot\text{m}^{-2}$; I is unit tensor.

2.5.3. Energy Equation

The energy conservation equation can be expressed as:

$$\frac{\partial(\rho T)}{\partial t} + \text{div}(\rho u T) = \text{div} \left(\frac{k}{c_p} \text{grad} T \right) + S_T \quad (8)$$

where T is temperature/K; k is heat transfer coefficient/ $\text{W}\cdot\text{m}^{-2}$; c_p is specific heat capacity at constant pressure/ $\text{J}\cdot\text{kg}^{-1}\cdot\text{K}^{-1}$; S_T is viscous dissipation term.

The conservation of mass of the components in a chemical reaction can be expressed as:

$$\frac{\partial(\rho Y_i)}{\partial t} + \nabla \cdot (\rho \vec{v} Y_i) = -\nabla \cdot \vec{J}_i + R_i + S_i \quad (9)$$

where Y_i is mass fraction of component i ; J_i is diffusive flux of component i ; R_i is net production rate of component; S_i is other source terms.

2.5.4. Realizable k- ϵ Equation

Considering the actual operating conditions of this burner, as well as the calculation efficiency and accuracy, the following Realizable k- ϵ model is used to conduct numerical simulations of the turbulence process:

$$\frac{\partial}{\partial t}(\rho k) + \frac{\partial}{\partial x_i}(\rho k u_j) = \frac{\partial}{\partial x_i} \left[\left(\mu + \frac{\mu_t}{\sigma_k} \right) \frac{\partial k}{\partial x_j} \right] + G_k + G_b - \rho \epsilon - Y_M + S_k \quad (10)$$

$$\frac{\partial}{\partial t}(\rho \epsilon) + \frac{\partial}{\partial x_j}(\rho \epsilon u_j) = \frac{\partial}{\partial x_i} \left[\left(\mu + \frac{\mu_t}{\sigma_\epsilon} \right) \frac{\partial \epsilon}{\partial x_j} \right] + \rho C_1 S_\epsilon - \rho C_2 \frac{\epsilon^2}{k + \sqrt{v \epsilon}} + C_{1\epsilon} \frac{\epsilon}{k} C_{3\epsilon} G_b + S_\epsilon \quad (11)$$

$$C_1 = \max \left[0.43, \frac{\eta}{\eta + 5} \right] \quad (12)$$

$$\eta = S \frac{k}{\epsilon} \quad (13)$$

In which G_k is the turbulent kinetic energy due to the laminar velocity gradient, G_b is the turbulent kinetic energy due to buoyancy, Y_M is the fluctuation due to over diffusion in compressible turbulence, $C_{1\epsilon} = 1.44$, $C_2 = 1.9$, σ_k and σ_ϵ are the turbulent Prandtl numbers for the k and ϵ equations, and S_k and S_ϵ are the custom source terms.

2.6. Numerical Simulation Method

Numerical simulation of the modelled 40 kW burner is carried out using ANSYS FLUENT (version 19.2) to verify the reliability of the selected models. The performance of the 14 MW burner prototype is then numerically simulated. The Realizable k- ϵ model was chosen for gas phase flow simulation. The non-premixed combustion model was chosen to calculate the reaction process, and the P1 radiation model was chosen to simulate the radiative heat transfer process. The pressure-velocity coupled calculation model is the SIMPLE algorithm, the discrete format is the second-order windward format, and the pressure correction equation is the PRESTO! algorithm. The wall surface of the combustion chamber is a no-slip wall surface.

3. Experimental Results and Discussion

3.1. Novel Gas Burner Performance Overview

3.1.1. Aerodynamic Field Characteristics

As shown in Figure 6, the experimental results reveal that the high-speed center jet expelled from the No. 1 gas nozzle heightens the velocity along the center axis at the $X = 0.0$ cross-section. This center jet elevates the gas flow's rigidity, enhancing its stability and consequently stabilizing flame combustion. The bend design of the No. 2 gas pipe not only facilitates the formation of a radial distribution of uniform gas spouting at the burner outlet cross-section but also acts as a turbulence-induced disturbance on the blunt body, reinforcing gas flow and thereby promoting gas–air mixing. With a continued increase in R , owing to the absence of gas pipe obstruction, the peripheral DC air can smoothly enter the combustion chamber, thereby augmenting the peripheral velocity at the burner nozzle. Increasing the airflow's peripheral velocity can further fortify jet stability. However, the intensified peripheral DC jet may impede outward expansion of the intermediate cyclone wind, reducing the jet's overall expansion angle.

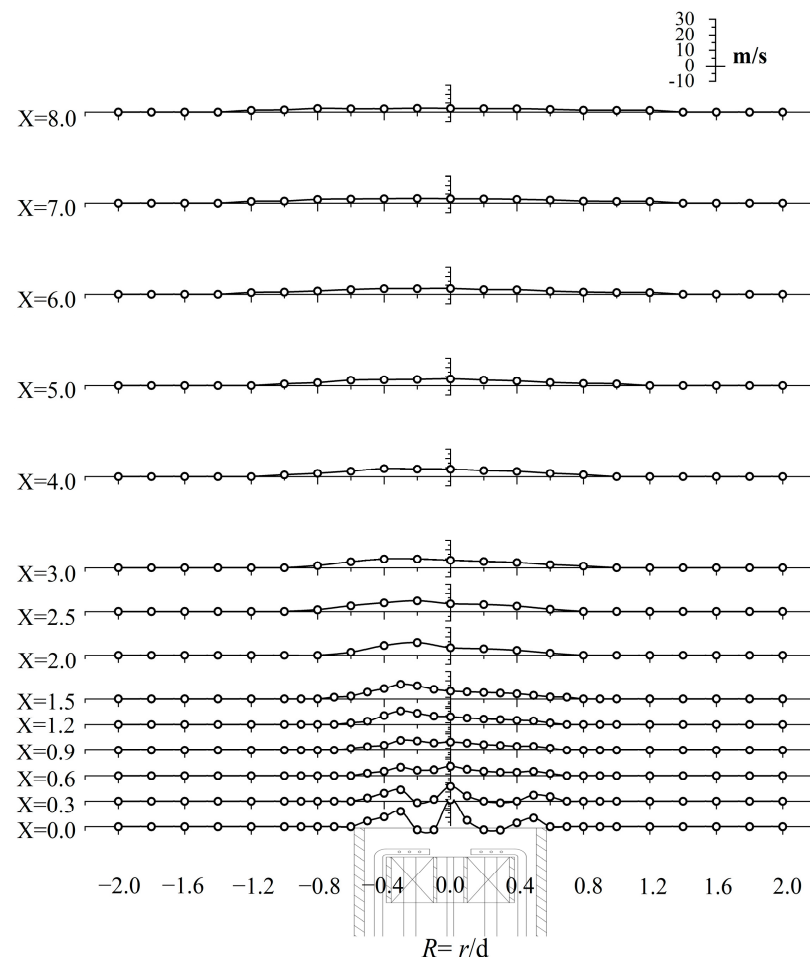


Figure 6. Aerodynamic field distribution of baseline test condition 0000.

As X increases, the velocity distribution gradually flattens. At the $X = 2.0$ cross-section, the aerodynamic field distribution resembles a non-isosceles triangle, with higher velocities observed on the left side of the center axis compared to the right side. This disparity arises because, within the range of $R < 0$, the No. 3 and No. 4 gas nozzles are oriented towards the measurement plane, while within the range of $R > 0$, they are directed away from it. The high-speed gas flow ejected from the No. 3 and No. 4 gas nozzles reaches the measurement plane, increasing the mass flow rate in the $R < 0$ range, thereby generating a localized

high-speed zone. Consequently, a velocity distribution characterized by high velocity on one side and low velocity on the other side is established within the range of $1.2 < X < 3.0$.

3.1.2. Gas Concentration Distribution Characteristics

As seen in Figure 7, the experimental results show that the gas is uniformly distributed overall, yet significant fluctuations in the gas distribution occur in front of the burner outlet ($-0.5 < R < 0.5$, $0.0 < X < 0.4$). Gas expelled from the No. 1 gas pipe amplifies the gas concentration at the center axis of the $X = 0.0$ cross-section, leading to an increase in Φ . Timely interception of the gas post-ejection aids in flame stabilization and prevents flameout.

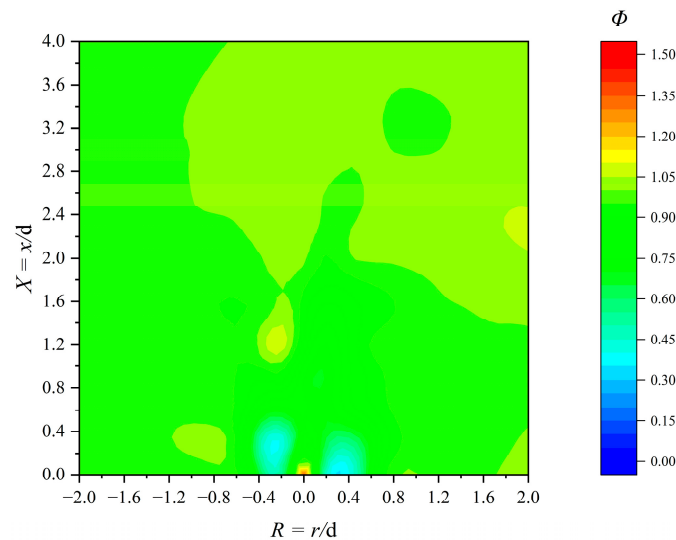


Figure 7. Dimensionless fuel–air ratio distribution cloud map of baseline test condition 0000.

The reduced gas concentration on both sides of the center axis in the $X = 0.0$ cross-section stems from the higher airflow in this region and the lower gas volume emitted from the No. 2 gas pipe, which constitutes approximately 19.57% of the total gas volume. The gas concentration increases again at around $R = -0.5$ and $R = 0.5$, which are located at the burner outlet's edge where the peripheral DC air exits. No. 3 and No. 4 gas pipes are arranged within the peripheral DC air duct, with gas emitted from these branches accounting for roughly 77.03% of the total gas volume. Consequently, in the burner outlet cross-section ($X = 0$, $-0.5 < R < 0.5$), the gas distribution exhibits a ring-shaped layered pattern: denser in the center, lighter in the middle, and moderate at the periphery. On both sides of the burner outlet ($R < -0.5$, $R > 0.5$), gas and air are thoroughly mixed. During the cold test, gas and air enter the combustion chamber without combustion, simulating mixing in a confined space. Thus, this analysis primarily focuses on the burner vicinity and the mixing of gas and air near the combustion chamber's center axis.

Along the axial direction, the mixing of gas and air gradually becomes more uniform. As the jet distance increases, a phenomenon of localized increase in dimensionless fuel–air ratio occurs in the range of $1.1 < X < 1.4$, $-0.4 < R < -0.1$, corresponding to the previously mentioned local high-velocity region. This analysis suggests that high-velocity gas ejected from No. 3 and No. 4 gas pipes, with nozzles facing the measurement plane, raises the gas concentration in this area, potentially leading to localized heat release from the flame and consequently an increase in temperature. The resulting localized high-temperature zone could significantly boost NO_x generation, compromising the burner's overall low NO_x emission performance. Hence, appropriate measures must be implemented to mitigate or eliminate localized gas buildup.

3.2. Effect of β on the Burner Aerodynamic Field and Gas Concentration Field

3.2.1. Aerodynamic Field Characteristics

As seen in Figure 8, the experimental results show that the distribution characteristics of the aerodynamic field of each burner in test condition group 1 are similar on the whole. Adjusting β mainly affects the high-speed region of the burner aerodynamic field.

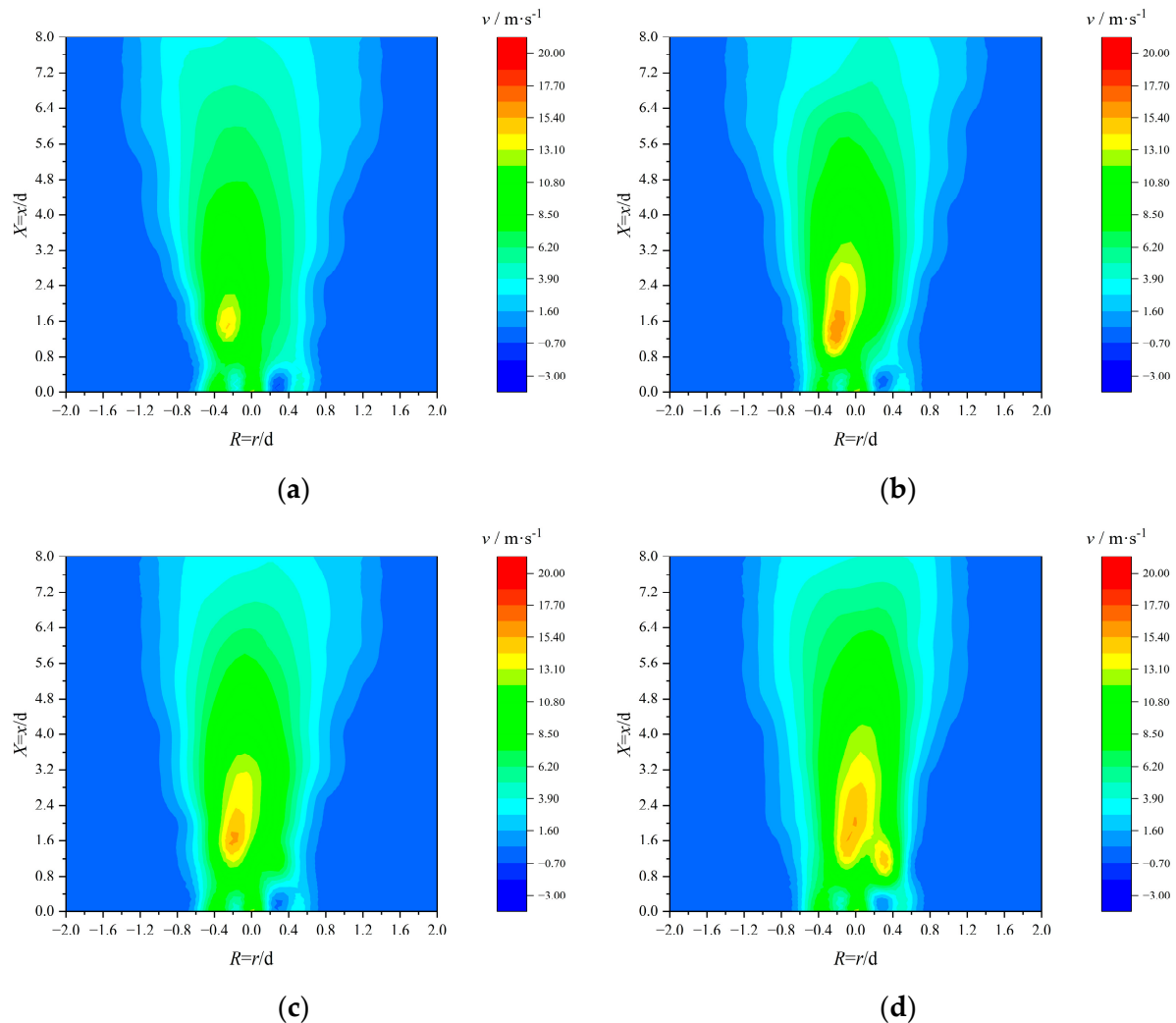


Figure 8. Aerodynamic field cloud map of each burner in test condition group 1. (a) 0000; (b) 0101; (c) 0102; (d) 0103.

The cross-section maximum dimensionless velocity can reflect the decay of the jet velocity with jet distance. In Figure 9, the maximum dimensionless velocity increases in the cross-section region of $1.0 < X < 1.5$, which is caused by the high-speed gas jet from the No. 3 gas pipe. In cases 0101, 0102, and 0103, β has the effect of penetrating the cyclone airflow layer. This structure strengthens the mixing and increases the mass flow rate of the center gas stream, which is conducive to improving the rigidity of the jet, and slows down the decay of the maximum velocity compared to Case 0000 (original structure).

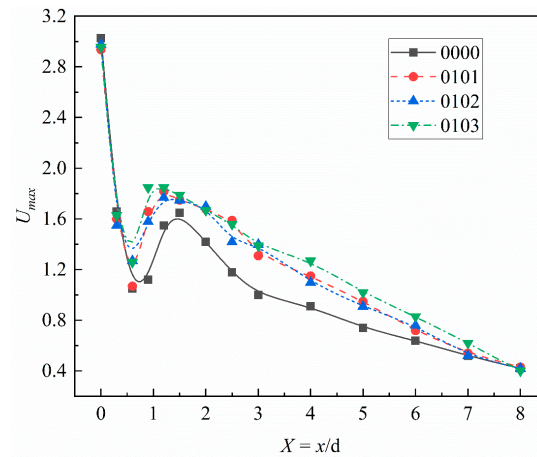


Figure 9. Trend of the maximum dimensionless axial velocity for each burner in test condition group 1.

3.2.2. Gas Concentration Distribution Characteristics

In Figure 10, the experimental results reveal that the fluctuation in gas concentration between $1.0 < X < 2.0$ becomes progressively sharper with increasing β . A comparison between gas concentration and aerodynamic field distributions reveals their consistent characteristics. This observation also suggests that excessively aggregating the gas' high-velocity jet trajectories may result in local gas concentration increases.

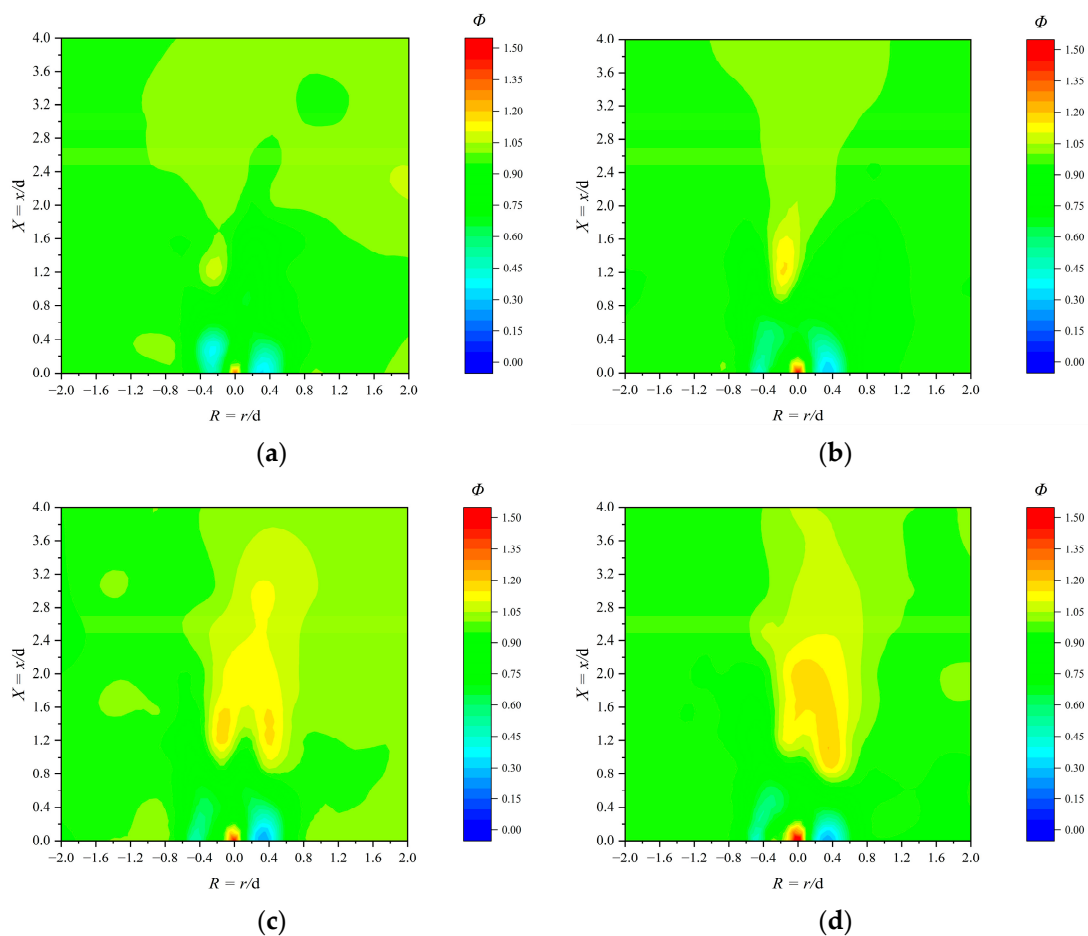


Figure 10. Dimensionless fuel–air ratio distribution cloud map for each burner in test condition group 1. (a) 0000; (b) 0101; (c) 0102; (d) 0103.

As shown in Figure 11, there exists a negative correlation between the fluctuation in Φ and the uniformity index. Within the range of $0.6 < X < 2.0$, the uniformity index generally exhibits an upward trend, despite the increased Φ fluctuation which is attributed to local gas aggregation from the No. 3 gas pipe injection. This suggests that local gas aggregation has a minimal effect on global gas mixing. At the $X = 4.0$ cross-section, the uniformity index exceeds 0.97, signifying sufficient mixing of gas and air. The structural design of this new burner enables an excellent mixing of gas and air.

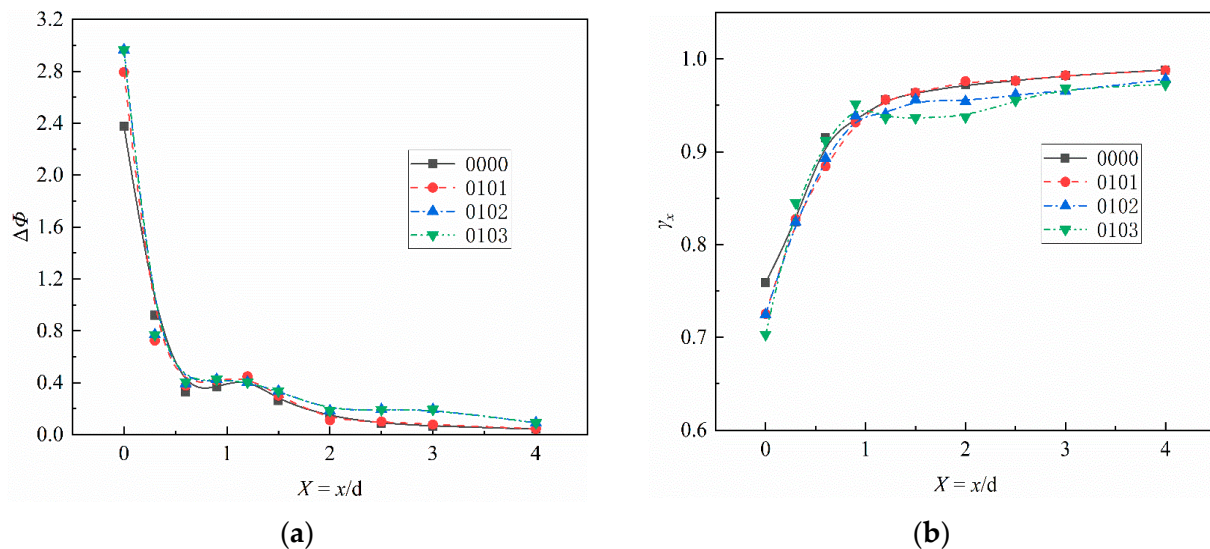


Figure 11. The trends in the dimensionless fuel–air ratio fluctuation amplitude and uniformity index along the axial direction in test condition group 1. (a) Dimensionless fuel–air ratio fluctuation amplitude; (b) uniformity index.

3.3. Effect of λ on the Burner Aerodynamic Field and Gas Concentration Field

3.3.1. Aerodynamic Field Characteristics

As shown in Figure 12, the No. 4 gas pipe possesses a larger nozzle bend angle, causing the gas jet trajectory to approach the burner outlet cross-section. Consequently, adjusting λ leads to a more significant alteration in velocity near the burner outlet.

Given that the gas flow rate of the No. 3 gas pipe comprises 56.64% of the total gas flow rate, whereas the gas flow rate of the No. 4 gas pipe constitutes 20.39%, the momentum of the gas ejected from the No. 3 gas pipe is higher when the jet velocity remains constant. Therefore, adjusting the deflection angle of the No. 3 gas pipe exerts a more pronounced effect on the aerodynamic field.

3.3.2. Gas Concentration Distribution Characteristics

In Figure 13, the gas concentration near the center axis gradually increases as the angle of the No. 4 gas pipe nozzle moves inward. For example, at the measurement point of $X = 0.3$ and $R = 0.0$, when λ increases from 15° to 90° , Φ increases from 1.30 to 1.56. The trend in Φ also shows that adjusting λ mainly plays a controlling role in the spatial distribution of the gas in the front side of the burner outlet.

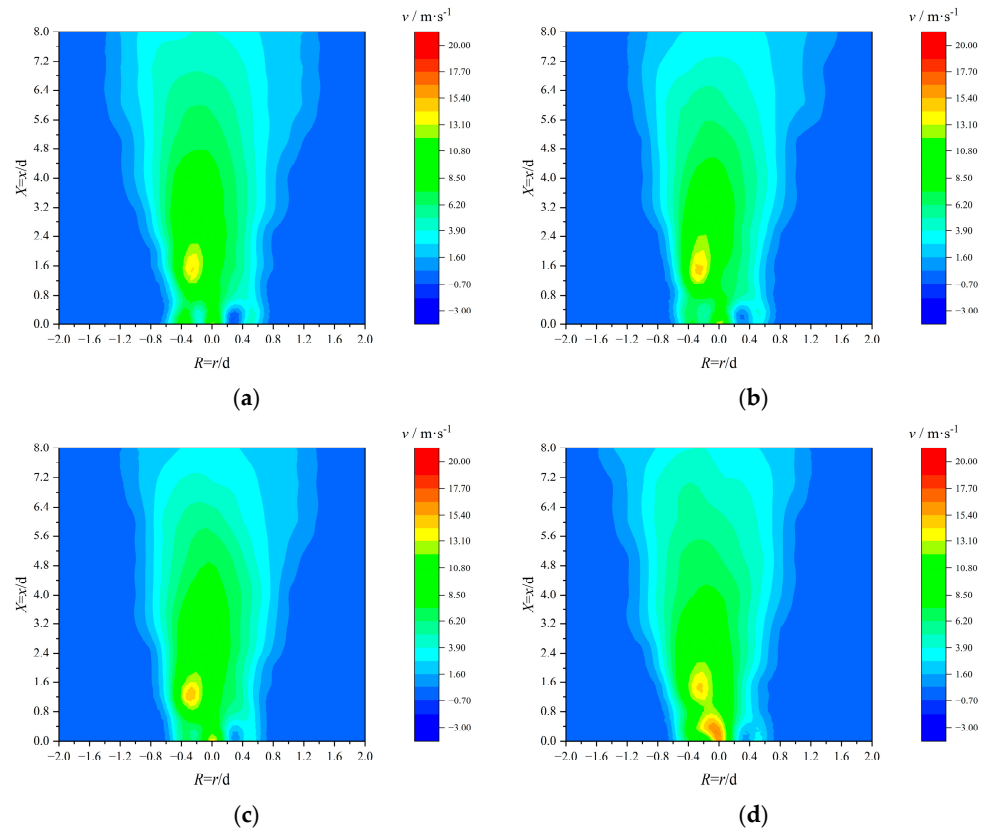


Figure 12. Aerodynamic field cloud map of each burner in test condition group 2. (a) 0000; (b) 0201; (c) 0202; (d) 0203.

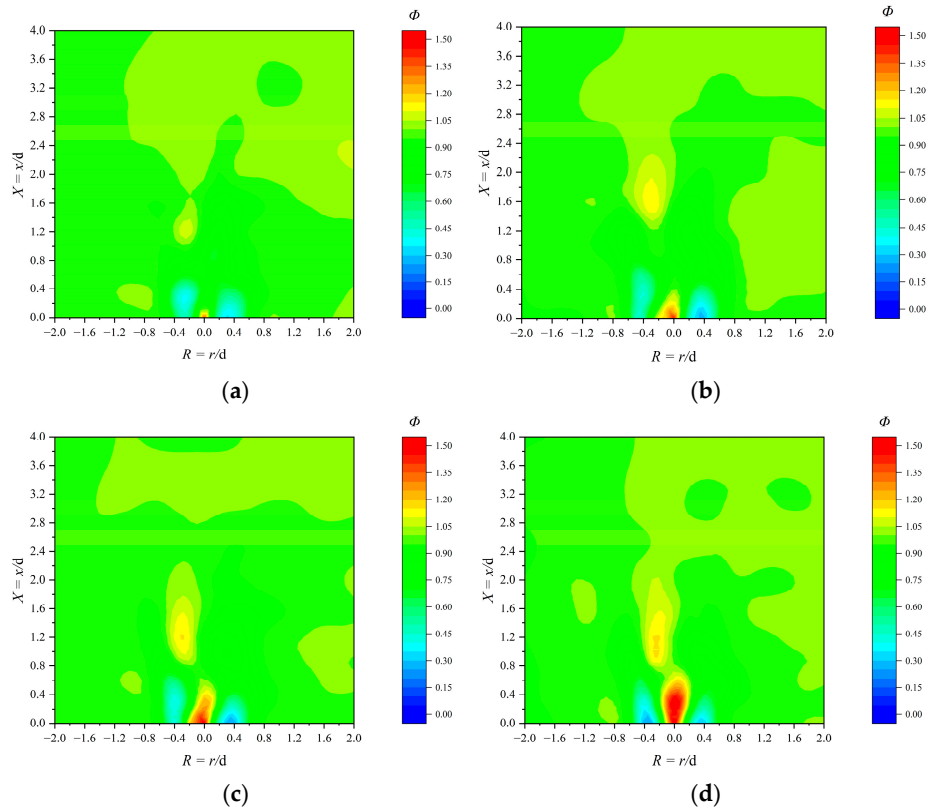


Figure 13. Dimensionless fuel–air ratio distribution cloud map for each burner in test condition group 2. (a) 0000; (b) 0201; (c) 0202; (d) 0203.

In Figure 14a, noticeable fluctuations in Φ occur within the range of $0.3 < X < 1.2$. The dimensionless fuel–air ratio fluctuation in the cross-section gradually increases with the rise in λ . Figure 14b depicts a consistent trend in the uniformity index of each burner. The index demonstrates a rapid increase with the augmentation of the jet distance within the range of $0.0 < X < 0.9$. Subsequently, the uniformity index stabilizes above 0.96 after the $X = 1.5$ cross-section, indicating a thorough mixing of gas and air.

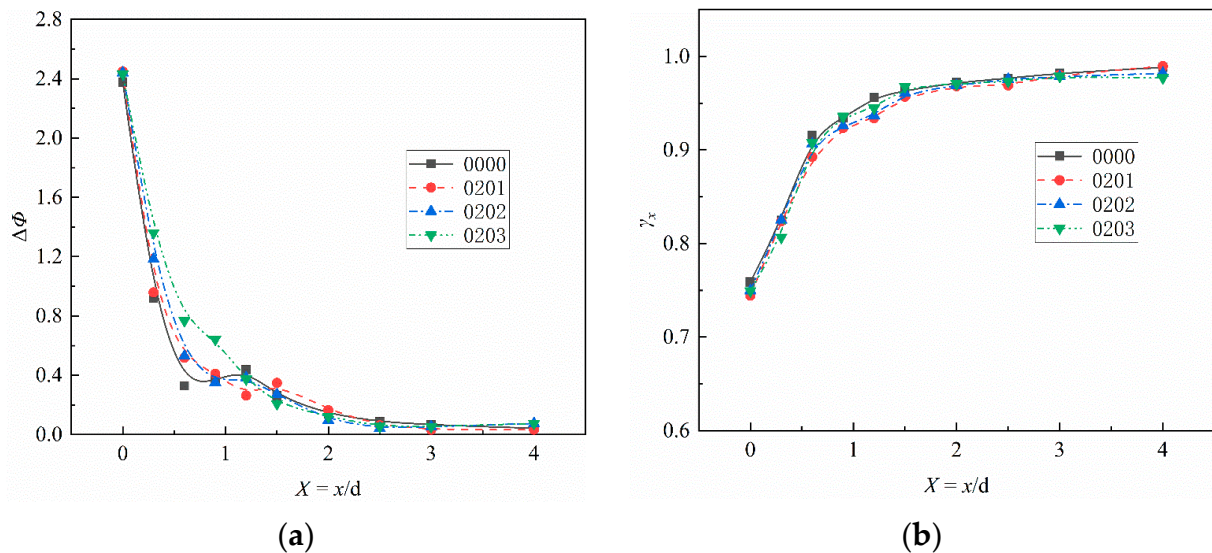


Figure 14. The trends in dimensionless fuel–air ratio fluctuation amplitude and uniformity index along the axial direction in test condition group 2. (a) Dimensionless fuel–air ratio fluctuation amplitude; (b) uniformity index.

3.4. Effect of α on the Burner Aerodynamic Field and Gas Concentration Field

3.4.1. Aerodynamic Field Characteristics

In Figure 15, α in Case 0301 is 0° , resulting in gas being injected perpendicular to the end surface of the combustion chamber. Each gas strand forms a parallel jet, lacking any velocity towards the measurement plane, leading to the absence of a high-velocity region. Compared with the other test conditions, a larger α brings the trajectory of the gas jet closer to the burner outlet, causing the high-velocity region to gradually shift towards the burner outlet cross-section.

As shown in Figure 16, increasing the bending angle of the No. 3 gas pipe enhances the maximum velocity of the burner's aerodynamic field and shortens the distance from the location of velocity extremum to the burner outlet.

3.4.2. Gas Concentration Distribution Characteristics

From Figure 17 it can be seen that the trend in Φ distribution mirrors that of the aerodynamic field. In Case 0301, where α is 0° and each gas flow forms a parallel jet, no significant gas aggregation area is evident in the measurement results. Additionally, the gas nozzle direction does not converge towards the center axis, resulting in a relatively low Φ at the outlet of the cyclone air and the peripheral DC air. As α increases, the gas aggregation area on the measurement plane gradually expands, shifting towards the upstream direction of the jet. This leads to a gradual increase in gas concentration near the burner outlet.

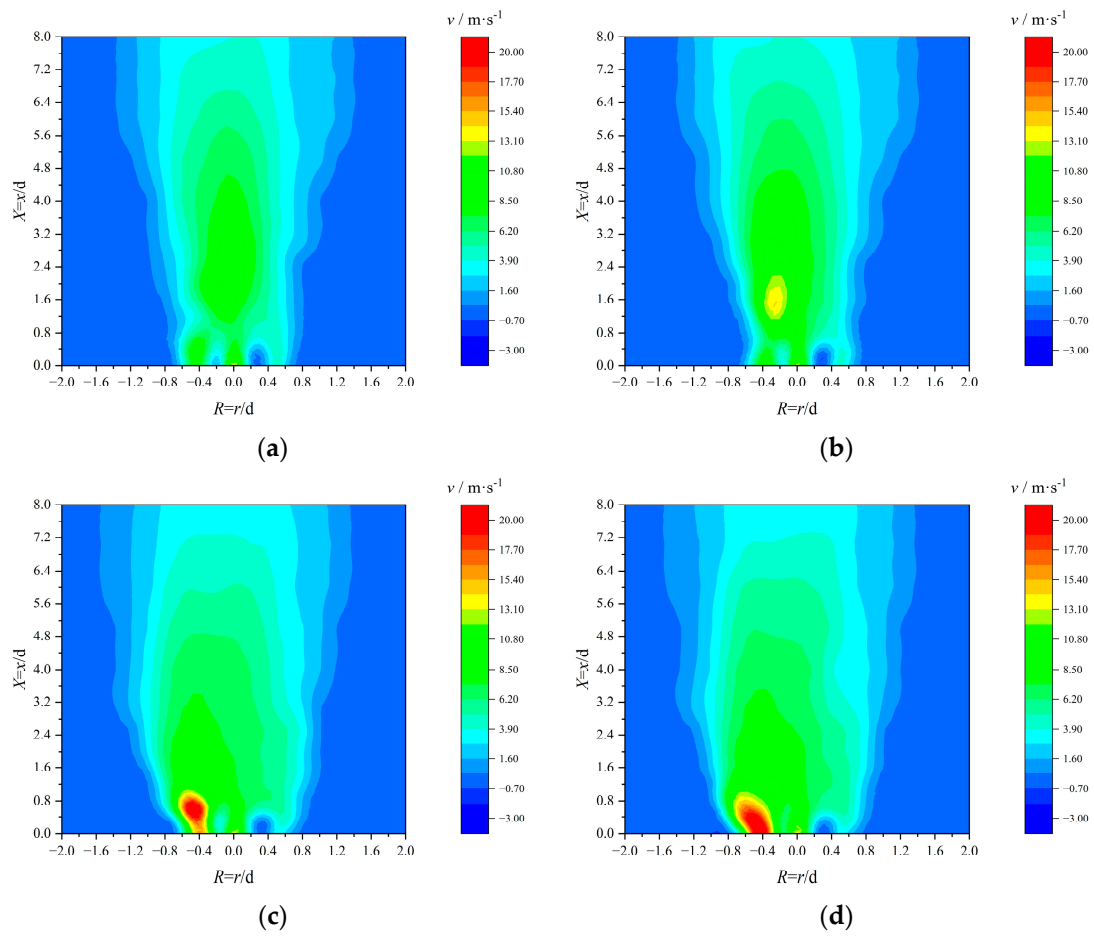


Figure 15. Aerodynamic field cloud map of each burner in test condition group 3. (a) 0301; (b) 0000; (c) 0302; (d) 0303.

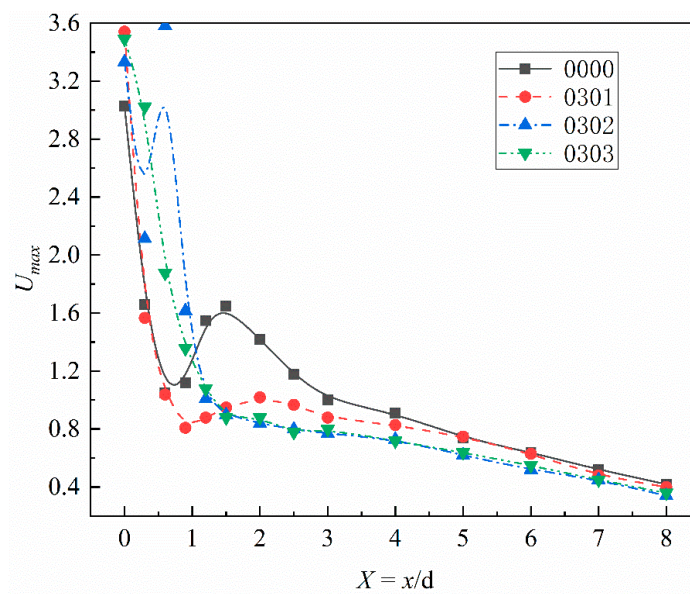


Figure 16. Trend of the maximum dimensionless axial velocity for each burner in test condition group 3.

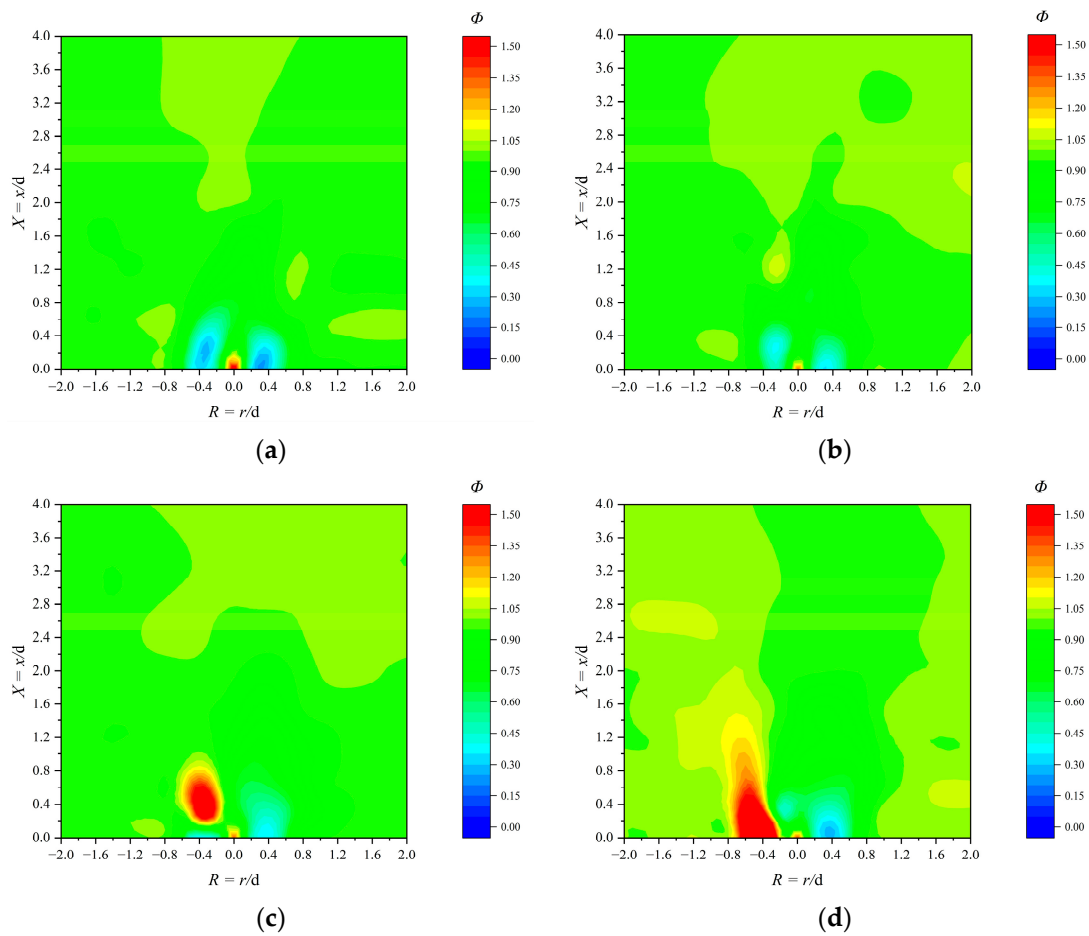


Figure 17. Dimensionless fuel–air ratio distribution cloud map for each burner in test condition group 3. (a) 0301; (b) 0000; (c) 0302; (d) 0303.

In Figure 18a it can be seen that an increase in α leads to a notable increase in the magnitude of Φ fluctuations within the range of $0.0 < X < 1.0$. In Case 0301, α decreases compared to Case 0000. However, the fluctuation of the dimensionless fuel–air ratio increases in the $X = 0$ section. This is due to a significant decrease in gas concentration at the outlet of the cyclone air and the peripheral DC air after α is changed to 0° , resulting in a decrease in the minimum value of Φ at the $X = 0$ cross-section.

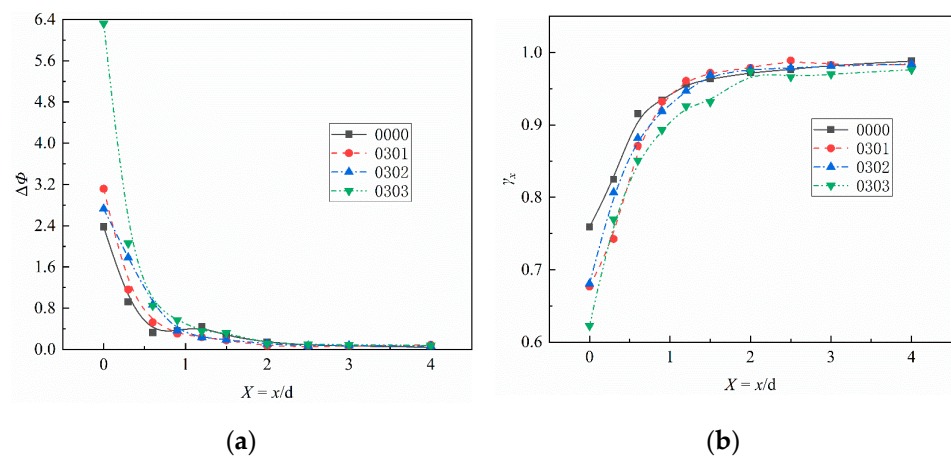


Figure 18. The trends in dimensionless fuel–air ratio fluctuation amplitude and uniformity index along the axial direction in test condition group 3. (a) Dimensionless fuel–air ratio fluctuation amplitude; (b) uniformity index.

Figure 18b illustrates a decrease in gas–air mixing uniformity within the range of $0.0 < X < 1.0$ due to the exacerbated dimensionless fuel–air ratio fluctuations mentioned earlier. However, in the interval of $1.0 < X < 3.0$, the uniformity index of Case 0301 surpasses that of Case 0000. This difference arises from the reduction in α , which mitigates the degree of local gas aggregation.

3.5. Effect of θ on the Burner Aerodynamic Field and Gas Concentration Field

As depicted in Figure 19, the gas flow through the No. 4 gas pipe is relatively minimal compared to the No. 3 gas pipe. Consequently, changes in the bending angle of the No. 4 gas pipe have a smaller impact on the aerodynamic field. Increasing the bending angle of the gas pipe nozzle results in a gradual shift towards convergence on one side and divergence on the other, leading to an asymmetric distribution of the aerodynamic field near the burner outlet with a high velocity on one side and a low velocity on the other. Similarly to the effect of θ on the aerodynamic field, adjustments to θ have minimal effects on the gas concentration distribution. The Φ distribution exhibits little change under varying bending angle conditions.

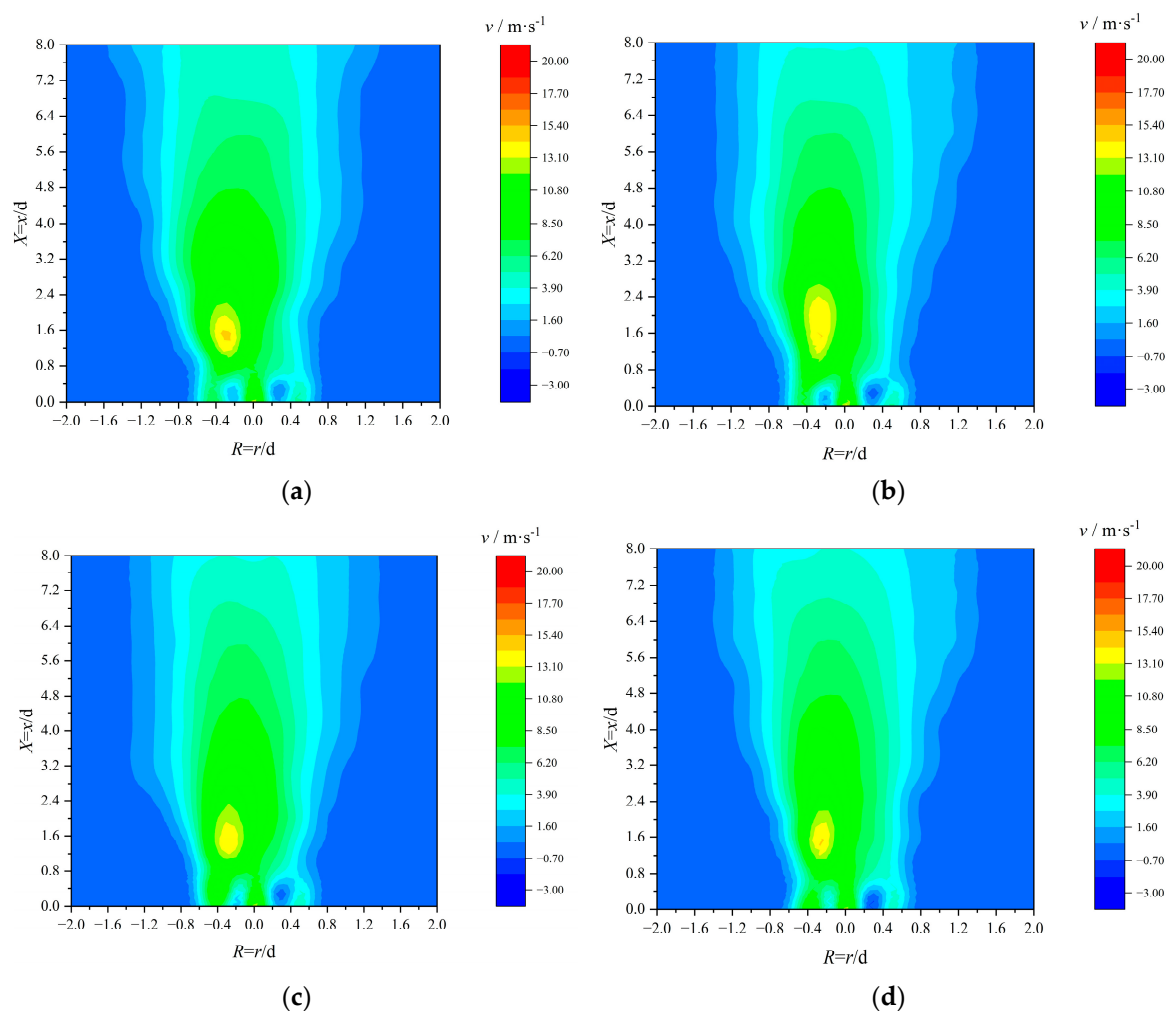


Figure 19. Aerodynamic field cloud map of each burner in test condition group 4. (a) 0401; (b) 0402; (c) 0403; (d) 0000.

3.6. Recommended Burner Design and Structure

Increasing the deflection angle or bending angle of the No. 3 gas pipe leads to a localized increase in the Φ of the gas near the burner outlet. An analysis and comparison of the test data under various test conditions suggest that β should be set at 0° and α at 0° .

Due to differences in gas flow size, adjusting the angle of the No. 4 gas pipe has a lesser influence on the aerodynamic field of the burner. However, to prevent cross superposition of gas jet trajectories from the No. 4 and No. 3 gas pipes and to enhance gas jet dispersion, it is recommended that λ be set to 15° and θ to 30° . The recommended design structure is illustrated in Figure 20.

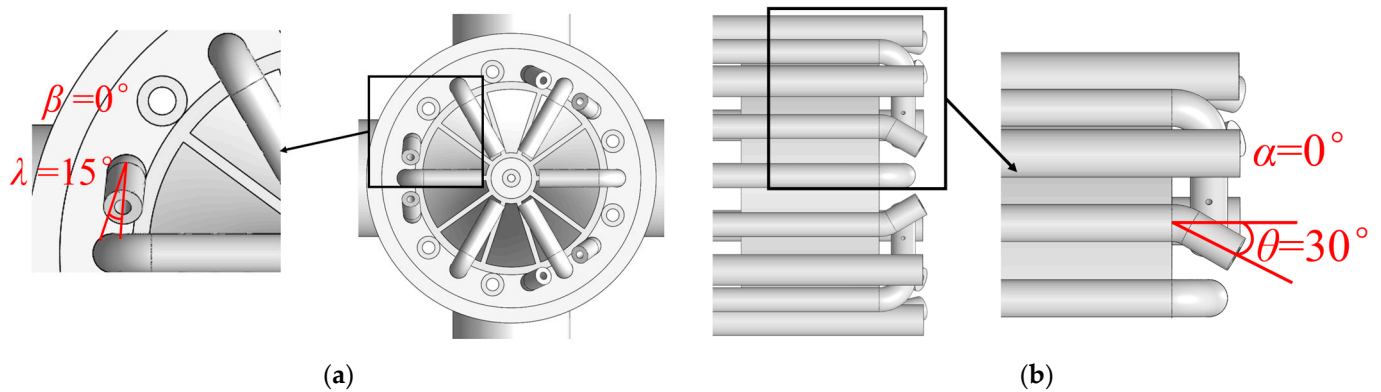


Figure 20. Schematic diagram of recommended design structure for the burner. (a) Gas pipe deflection angle; (b) gas pipe bending angle.

3.7. Analysis of Numerical Simulation Results

3.7.1. Validation of Numerical Simulation against Experiment

The 40 kW burner model was simulated with a cold flow field. The boundary conditions are the same as the test conditions. As shown in Figure 21, both the numerical simulation data and the test data exhibit similar trends in the dimensionless velocity distribution curve and the dimensionless fuel–air ratio distribution curve along the central axis of the combustion chamber. In general, the simulation results of the model have the same trend as the test results, and the data are close to each other, so the numerical simulation results have high reliability.

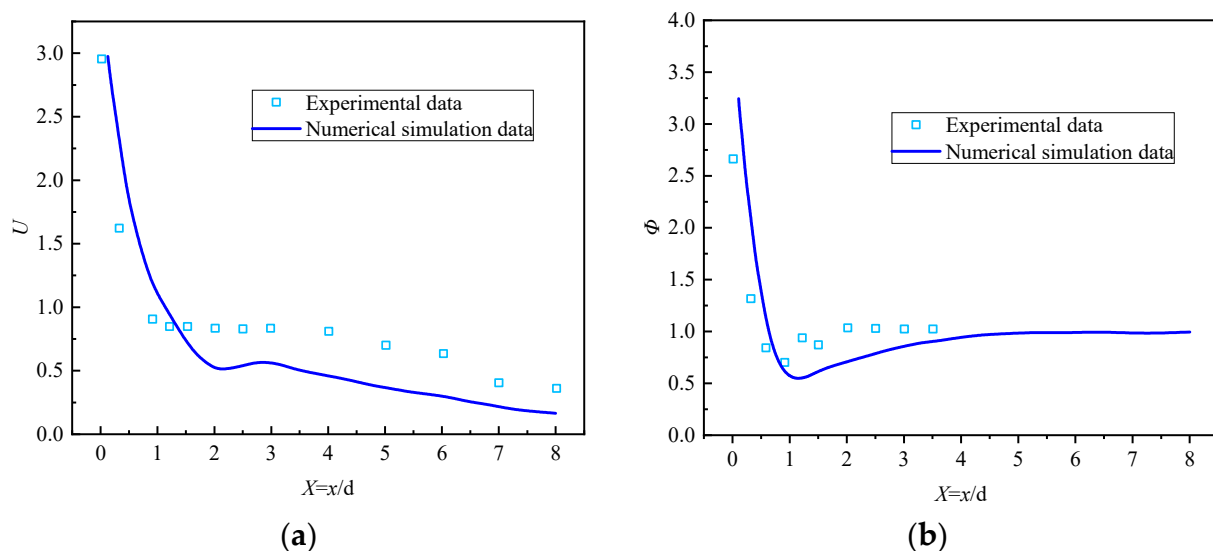


Figure 21. Comparison of trends between numerical simulation data and experimental data. (a) Comparison of dimensionless velocity trends; (b) comparison of the trends in dimensionless fuel–air ratios.

3.7.2. Numerical Simulation Analysis of 14 MW Burner

As shown in Figure 22a, the gas ignites quickly upon nozzle ejection, forming a stable flame. The unique nozzle arrangement creates a continuous flame belt at the combustion chamber entrance, enhancing combustion stability and uniform flame temperature.

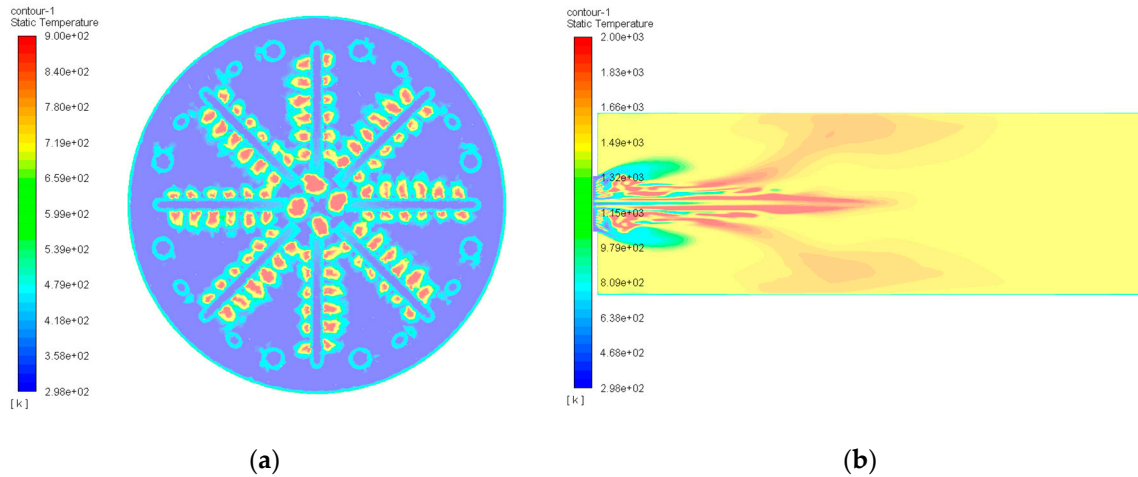


Figure 22. Temperature distribution cloud. (a) Temperature distribution cloud of burner nozzle cross section; (b) cloud view of flue gas temperature distribution in the combustion chamber.

In Figure 22b, the temperature field is oriented along the central axis direction which shows that the gas injected from the No. 1 pipe burns steadily, forming a central sharp needle-like flame, namely the combustion core zone. Partial intermediate products such as CO and OH continue to burn in the midstream of the combustion chamber, forming the band-like flame area. In the downstream of the combustion chamber, the flue gas temperature gradually tends to be uniform, and the average temperature of the flue gas is about 1622.23 K.

The NO_x produced during the combustion process is mainly in the form of NO with negligible NO_2 content. As shown in Figure 23, higher temperatures in the combustion core resulted in thermal NO production at a concentration around 39.5 mg/m^3 . With the mixing of the cyclonic air, the NO concentration gradually decreases. The NO distribution downstream of the combustion chamber tends to be uniform, and the original NO concentration at the exit cross-section of the combustion chamber is about 17.00 mg/m^3 (3.5% oxygen content).

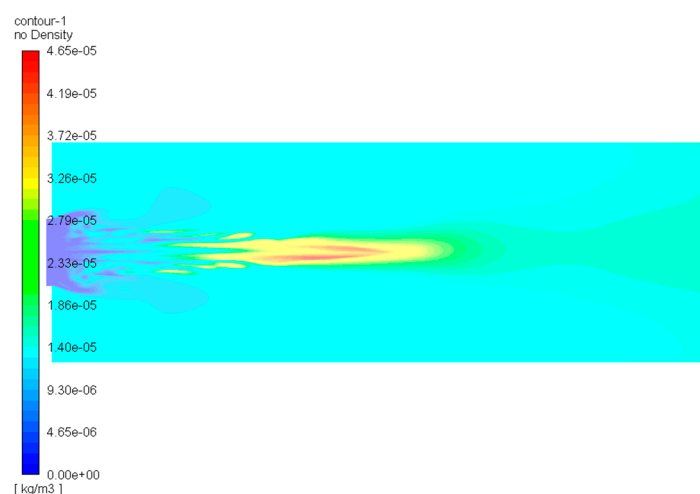


Figure 23. NO concentration distribution cloud.

4. Conclusions

This paper examines the performance of a novel low-NO_x burner utilizing gas-dispersed jet and air cyclone coupling technology in cold conditions. It delves into the impact of the burner's structural parameters on the aerodynamic field, gas–air mixing characteristics, and low-NO_x combustion performance. The main conclusions drawn from this study are outlined as follows:

- (1) The angle of the No. 3 and No. 4 gas pipes has a significant impact on the aerodynamic field and gas concentration field of the burner. Increasing β or λ causes the high-velocity zone and high-concentration zone of the flow field to shift towards the center axis direction; conversely, decreasing these angles shifts the zones towards the outer layer of the jet. Similarly, increasing α or θ shifts the high-velocity zone and high-concentration zone towards the upstream direction of the jet, while decreasing these angles shifts the zones towards the downstream direction of the jet.
- (2) As the jet distance increases, the uniformity of gas–air mixing gradually improves. Local gas aggregation has a minimal impact on the overall mixing of gas and air in the flow field. When the dimensionless jet distance exceeds 1, gas and air achieve complete mixing, resulting in a cross-section uniformity index of over 0.95.
- (3) The simulation results show that the average temperature inside the combustion chamber is about 1622.23 K. The NO concentration at the exit of the combustion chamber is 17 mg/m³ (3.5% oxygen content), which meets the requirement of ultra-low NO_x emission.
- (4) Within the experimental test range, the optimal design structure of the burner consists of a deflection angle of 0° and a bending angle of 0° for the No. 3 gas pipe, and a deflection angle of 15° and a bending angle of 30° for the No. 4 gas pipe.

Author Contributions: Conceptualization, M.G. and S.J.; methodology, M.G. and S.J.; software, M.G.; validation, D.W., S.J., and M.G.; formal analysis, M.G. and S.J.; investigation, D.W.; resources, S.J.; data curation, M.G.; writing—original draft preparation, M.G. and S.J.; writing—review and editing, D.W. and M.G.; visualization, S.J.; supervision, D.W.; project administration, D.W. All authors have read and agreed to the published version of the manuscript.

Funding: This research received no external funding.

Institutional Review Board Statement: Not applicable.

Informed Consent Statement: Not applicable.

Data Availability Statement: Data available on request.

Conflicts of Interest: The authors declare no conflicts of interest.

References

1. Compais, P.; Arroyo, J.; Tovar, F.; Cuervo-Piñera, V.; Gil, A. Promoting the valorization of blast furnace gas in the steel industry with the visual monitoring of combustion and artificial intelligence. *Fuel* **2024**, *362*, 130770. [[CrossRef](#)]
2. Kim, S.; Kim, J. The optimal carbon and hydrogen balance for methanol production from coke oven gas and Linz-Donawitz gas: Process development and techno-economic analysis. *Fuel* **2020**, *266*, 117093. [[CrossRef](#)]
3. Mariños Rosado, D.J.; Rojas Chávez, S.B.; Amaro Gutierrez, J.; Mayworm de Araújo, F.H.; de Carvalho, J.A.; Mendiburu, A.Z. Energetic analysis of reheating furnaces in the combustion of coke oven gas, Linz-Donawitz gas and blast furnace gas in the steel industry. *Appl. Therm. Eng.* **2020**, *169*, 114905. [[CrossRef](#)]
4. Wen, S.; Zhou, K.; Lu, Q. A discussion on CBM development strategies in China: A case study of PetroChina Coalbed Methane Co., Ltd. *Nat. Gas Ind. B* **2019**, *6*, 610–618. [[CrossRef](#)]
5. Du, Y.; Xing, M.; Zhang, J.; Zhang, J.; Deng, L.; Che, D. Combustion characteristic of low calorific gas under pilot ignition condition—Exploring the influence of pilot flame products. *Fuel* **2023**, *333*, 126613. [[CrossRef](#)]
6. Paulauskas, R.; Skvorčinskienė, R.; Zakarauskas, K.; Striūgas, N. Combustion performance of low calorific gas enriched by oxygen and ozone. *Fuel* **2022**, *324*, 124761. [[CrossRef](#)]
7. Zhang, L.; Li, S.; Yao, M.; Zhou, H.; Ren, Z. Analysis of operating limits and combustion state regulation for low-calorific value gases in industrial burners. *Int. J. Hydrog. Energy* **2022**, *47*, 1306–1318. [[CrossRef](#)]

8. Shui, H.; Wang, Y.; Liu, Z.; Guo, W. Optimal parameter adjustment of catalytic combustion heaters for oil shale in-situ conversion of low calorific value gases. *J. Clean. Prod.* **2023**, *426*, 139020. [[CrossRef](#)]
9. Razzaq, R.; Li, C.; Zhang, S. Coke oven gas: Availability, properties, purification, and utilization in China. *Fuel* **2013**, *113*, 287–299. [[CrossRef](#)]
10. Yang, M.; Zhang, M.; Han, M.; Zhou, S. Coke oven gas utilization status and development direction. *Coal Mine Mod.* **2011**, *6*, 1–4. [[CrossRef](#)]
11. Agency, I.E. Tracking Industrial Energy Efficiency and CO₂ Emissions. *Int. Energy Agency* **2007**, *34*, 1–12.
12. Wang, Q.; Wang, E.; Li, X.; Hu, Z.; Liu, D.; Yu, Y. Numerical Investigation and Improvement of Coke Oven Gas-Fired W-Shaped Radiant Tubes for NO_x Reduction. *Energy Fuels* **2020**, *34*, 4925–4933. [[CrossRef](#)]
13. Yan, B.; Xue, C.; Ba, H.; Fan, H.; Li, F. Reviews on the Comprehensive Utilization of Coke Oven Gas. *Shandong Chem. Ind.* **2020**, *49*, 87–90. [[CrossRef](#)]
14. Zhou, J.-W. Analysis on Comprehensive Utilization Technology of Coke Oven Gas. *Chem. Eng. Des. Commun.* **2020**, *46*, 4–6. [[CrossRef](#)]
15. GB 13271-2014; Emission Standard of Air Pollutants for Boiler. China Environmental Press: Beijing, China, 2014.
16. DB 11/139-2015; Emission Standard of Air Pollutants for Boilers. Beijing Municipal Ecology and Environment Bureau: Beijing, China, 2015.
17. Zhang, L.; Xie, W.; Ren, Z. Combustion stability analysis for non-standard low-calorific gases: Blast furnace gas and coke oven gas. *Fuel* **2020**, *278*, 118216. [[CrossRef](#)]
18. Cai, S.; Zhang, L.; Pu, K.; Zhou, J. Experimental study on optimization of low calorific value coal bed methane burner structure. *J. Eng. Therm. Energy Power* **2012**, *27*, 202–206.
19. Bâ, A.; Cessou, A.; Marciano, N.; Panier, F.; Tsiava, R.; Cassarino, G.; Ferrand, L.; Honoré, D. Oxyfuel combustion and reactants preheating to enhance turbulent flame stabilization of low calorific blast furnace gas. *Fuel* **2019**, *242*, 211–221. [[CrossRef](#)]
20. Karyeyen, S.; Ilbas, M. Experimental and numerical analysis of turbulent premixed combustion of low calorific value coal gases in a generated premixed burner. *Fuel* **2018**, *220*, 586–598. [[CrossRef](#)]
21. Weiss, C.; Rieger, J.; Rummer, B. Formation and Control of Nitrogen Oxide in the Heating System of a Coke Oven. *Environ. Eng. Sci.* **2012**, *29*, 555–562. [[CrossRef](#)]
22. Zeldovich, I.A.B.; Barenblatt, G.I.; Librovich, V.B.; Makhviladze, G.M. *The Mathematical Theory of Combustion and Explosions*; Plenum Press: New York, NY, USA, 1985; 597p.
23. Merzhanov, A.G.; Sirignano, W.A.; Luca, L.D. *Advances in Combustion Science: In Honor of Ya. B. Zel'dovich*; American Institute of Aeronautics and Astronautics: Washington, DC, USA, 1997.
24. Zhong, Y. Formation mechanism and control of NO_x during coke oven heating and combustion. *Fuel Chem. Process* **2009**, *40*, 5–12. [[CrossRef](#)]
25. Cao, Y.; Du, Z.; Hu, Z.; Jin, S.; Lu, W.; Zhang, R. The Effects of the Size and Location of the Recirculation Windows of Combustion Chambers in a Coke Oven on Emissions of NO and Unburnt Fuels by CFD Numerical Simulation. *IOP Conf. Ser. Mater. Sci. Eng.* **2020**, *964*, 012006. [[CrossRef](#)]
26. Poraj, J.; Gamrat, S.; Bodys, J.; Smolka, J.; Adamczyk, W. Numerical study of air staging in a coke oven heating system. *Clean Technol. Environ. Policy* **2016**, *18*, 1815–1825. [[CrossRef](#)]
27. Paubel, X.; Cessou, A.; Honore, D.; Vervisch, L.; Tsiava, R. A flame stability diagram for piloted non-premixed oxycombustion of low calorific residual gases. *Proc. Combust. Inst.* **2007**, *31*, 3385–3392. [[CrossRef](#)]
28. Pei, Y.; Liu, Q.; Wang, C.; Wang, G. Energy efficiency prediction model and energy characteristics of subsea disc pump based on velocity slip and similarity theory. *Energy* **2021**, *229*, 120690. [[CrossRef](#)]
29. Zhang, W.; Chai, X.; Li, S. Research on Definition and Influential Factors for Smoke Temperature of the Furnace Outlet of the Horizontal Internal-combustion Oil-fired (Gas) Boiler. *Ind. Boil.* **2001**, *4*, 2–6. [[CrossRef](#)]

Disclaimer/Publisher's Note: The statements, opinions and data contained in all publications are solely those of the individual author(s) and contributor(s) and not of MDPI and/or the editor(s). MDPI and/or the editor(s) disclaim responsibility for any injury to people or property resulting from any ideas, methods, instructions or products referred to in the content.